Laser-Guided Microcanvas Printing of Multicolor Upconversion Nanoparticles on Molybdenum Disulfide Monolayer

Eng Tuan Poh, Xiaogang Liu,* and Chorng Haur Sow*

Scanning focused laser beams incident on nanomaterials have provided a nondestructive and facile technique to fabricate micropatterns of a wide variety of hybrid materials. Conventionally, the technique is limited to localized chemical modification or in situ reduction of specific metal ions en route to heterogeneous material systems. However, as hybrid structures continue to be an essential form to couple various material properties and bring forth nanostructures with designable traits, the need for a flexible technique to interface nanomaterials presynthesized in higher quality remains an important challenge. Herein, a technique for laser-guided microcanvas formation by anchoring preformed upconversion nanoparticles at specific sites on a MoS_2 monolayer surface is presented. The technique expands the building blocks in laser-produced hybrid structures to include presynthesized nanomaterials. The upconversion microstructures are formed via a microbubble-assisted mechanism, with distinct emission contrast against the background. The proof-of-concept production of a multicolor upconversion microcanvas marks the potential for full-color high-resolution displays while the technique opens up the possibility of fabricating an expandable range of new hybrid structures.

1. Introduction

The utility of laser beams on material formation and patterning has had a long lineage of extensive research explorations. From nanomaterial formation under the thermal influence of laser

E. T. Poh
Graduate School for Integrative Sciences and Engineering (NGS)
National University of Singapore
Singapore 119077, Singapore

E. T. Poh, Prof. C. H. Sow
Center For Advanced 2D Materials and Graphene Research Center
National University of Singapore
6 Science Drive 2, Singapore 117546, Singapore
E-mail: physowch@nus.edu.sg

Prof. X. Liu
Department of Chemistry
National University of Singapore
3 Science Drive 3, Singapore 117543, Singapore
E-mail: xiaogangliu@nus.edu.sg

Prof. C. H. Sow
Department of Physics
National University of Singapore
2 Science Drive 3, Singapore 117551, Singapore

The ORCID identification number(s) for the author(s) of this article can be found under https://doi.org/10.1002/admi.201901673.

ablation techniques,[1,2] to microwriting of photoresist patterns in conventional lithography,[3–6] lasers have played critical roles in driving local self-assemblies or chemical changes to produce desired micropatterns. Beyond these traditional techniques, focused laser beams coupled to low-cost microscopes have also been exploited for spatially directed, site-specific oxidation of various nanomaterials, as well as in situ production of a diverse range of nanostructures on photoactive substrates. Through a laser path directed into a metallurgical microscope, the setup produces laser writing systems flexible to accommodate variations in the laser excitation wavelength and the nature of the substrate materials. Furthermore, the avoidance of substrate pretreatment, mask alignment, and potential chemical contamination ascends the technique of direct laser writing in favor of conventional lithographic methods.

In the most fundamental operation of the direct laser writing technique, the focused laser beam incident on the sample provides sufficient thermal or photonic energy for the material to overcome the activation barrier and partake in site-specific local chemical changes. The first generation works demonstrated the capability for spatially refined removal of materials for patterning and crafting functional microstructures. These efforts include laser pruning of carbon nanotube arrays to produce 2D/3D microstructures[7] and high-efficiency quantum dot (QD) nanosieves,[8] laser vaporization of highly inert cross-linked SU-8 epoxies,[9] and localized combustion of porphyrin nanotubes (PNTs).[10] Beyond that, subsequent studies were tuned toward laser stimulated oxidation of various nanomaterials, including $GeSe_2$ nanostructures,[11] mesoporous silicon nanowires (mp-SiNWs),[12] CdS_xSe_{1-x} nanobelts,[13] and phosphorene nanofilms.[14,15] These works not only explored the rich chemistry and physics at play on the local scale, but also resulted in the formation of highly functional photodetectors and chemical sensors.

On 2D materials, the laser was found to affect these photoactive thin layers differently, providing controlled alterations to the inherently unique optical and chemical natures of the layer surfaces.[16] More importantly, the laser-induced chemical change could produce regional catalytic microsites capable of subsequent reduction of Au^{3+} ions to Au nanoparticles

**ADVANCED
SCIENCE NEWS**
www.advancedsciencenews.com

**ADVANCED
MATERIALS
INTERFACES**
www.advmatinterfaces.de

(AuNPs), presenting patterned hybrids of AuNP-decorated rGO[17] and MoS_2[18,19] for sensitive surface-enhanced Raman spectroscopy of various adsorbed organic moieties. However, the use of a two-step process—laser modification followed by Au^{3+} ion exposure is typically hindered by nonuniform coverage of AuNPs over a broad size range. To overcome these limitations, Teoh et al. devised a single step process to direct the laser upon an rGO surface emplaced within a solution cell of ethanolic $AgNO_3$, resulting in situ formation and refined anchoring of AgNPs onto the substrate.[20] Further expansion of the technique to permutations of metallic nanoparticles and variable substrates produced AgNP–alumina veil,[21] AgNP–GO,[22] and AlNP–GO[23] hybrids capable of the respective applications in steganographic transmission, tricolor optical blinkers, and patterned blue fluorescing templates. Analogous to the examples above, the laser-induced chemical liquid phase deposition technique has also been used to deposit various metals as functional electrodes on polymer substrates. However, this technique has been limited to operations specifically involving metal precursors in various reducing electrolytes.[24,25]

Despite the capability to synthesize nanomaterial hybrids under the facile, clean, and low-cost operation, however, it is worthy to note that the modulus of such operation is typically constrained to metal ion species that can be much easily reduced under the photoactivated electron generation from the underlying 2D material. By contrast, the potential of the laser technique to assemble preformed nanostructures has yet to be fully developed. By expanding the technique to preformed nanomaterials, it provides the option to work with nanostructures presynthesized in higher quality to form caliber microstructured hybrids with better controlled functionality. Furthermore, it allows for hybrid interface with nanostructures of complex material composition such as upconversion nanoparticles (UCNPs), NPs of transitional metal dichalcogenides (TMD NPs), and semiconductor QDs that cannot be produced under a laser irradiated reduction process. Such an expansion would cater to a greater variety of hybrid materials in order to establish more complex and functional hybrid devices.

Scientific development in recent years has brought the spotlight upon hybrid structures involving lanthanide nanomaterials and TMDs, owing to the expansion of study in both fields over the past 10 years. These hybrids have demonstrated their capabilities as FRET-based biochemical sensors for DNA[26] and microcystin-LR[27] detection, wavelength selective photodetectors,[28–30] photocatalysts,[31] and memory devices.[32] However, these structures are usually interfaced by drop cast and spin-coating techniques or preformed as nanostructures during the synthesis regime, providing little control over spatial extent for hybrid formation. Beyond that, advanced lithographic[33] and various printing techniques[34–37] have provided spatial control in the patterned formation of such hybrid structures. Nonetheless, the need for the much more expensive and sophisticated instrumentation, along with the hazardous incompatibility of the solvents may prove an issue for day to day operations.

Herein, we present laser-assisted deposition of preformed UCNPs onto MoS_2 monolayers at high spatial resolution. Through the use of the focused laser beam, UCNPs were deposited in situ directly from the colloidal suspension, producing ring- and sponge-like microstructures arising from nanoparticle aggregation. The technique offers noncontact operation with resolution down to the micrometer scale. Along with enhanced selectivity for the monolayer in place of the underlying silicon substrate, the hybrid presents a highly defined upconversion pattern of stark contrast relative to the weak background. The method is not only universal to various polar solvents and laser wavelengths but also allows for repeated deposition of UCNPs with different emission profiles, resulting in low-cost production of a multicolor microdisplay.

2. Results and Discussion

2.1. Synthesis and Characterization of Hybrid Components: UCNPs and MoS_2 Monolayer

Figure 1a demonstrates the overall schematics to the experimental design leading up to the formation of the micropatterned UCNP/MoS_2 hybrids. Depicted under Figure 1b, a laser beam is directed into the metallurgical microscope, by means of mirror optics, through a route parallel to that of the optical light path. The beam is focused onto the sample surface with a radial width of ≈1 µm. Coupled with a sample stage microcontroller, the refine control allowed for precise single laser spot positioning and relative movement critical for the subsequent microcanvas printing process. In order to favor dynamic UCNP movement and aggregation driven by the laser beam, the substrate is topped with a homemade solution containment cell as presented under Figure 1c. The containment cell comprises a rectangular frame carved out of PDMS mold, with the center void containing a colloidal suspension of the designated nanoparticles enclosed with a thin glass slide above. This allows for in situ laser-induced nanoparticle aggregation and microscale canvas formation amidst a colloidal environment of fairly consistent volume and concentration, prompting high-resolution patterning of UCNP/MoS_2 hybrids.

In this work, UCNPs were synthesized by a standard coprecipitation method well-established in the literature.[38,39] With a large selection of dopant and host variants, the versatility to engineer UCNPs could cater to specific control over its optical properties. The intricate design of the core–shell forms of $NaYF_4$ and $NaGdF_4$ nanoparticles dictate the transfer pathway of the absorbed 980 nm NIR photon, from the highly absorbing "sensitizer" species to the emitting "activator" ions.[43] This is achieved by exploiting the respective energy transfer upconversion[40,41] and energy migration upconversion mechanisms[42] (Figure S1a,b, Supporting Information). Through the use of various lanthanide activator ions (Er^{3+}, Tb^{3+}, Eu^{3+}) coupled with the corresponding host particle design, we produced three UCNP types with disparate emission profiles and colors (Figure S1c–e, Supporting Information) for this study.

The typical characteristics of the as-synthesized UCNPs were demonstrated through the SEM and TEM analyses (Figure S1h,i, Supporting Information). The UCNPs were assessed to be of great quality due to its high dispersity, narrow size distribution, and uniform shapes. The UCNPs were presented as hexagonal platelets of 20–30 nm each, providing an accurate reflection of the sixfold symmetry arising from the $P6_3/m$
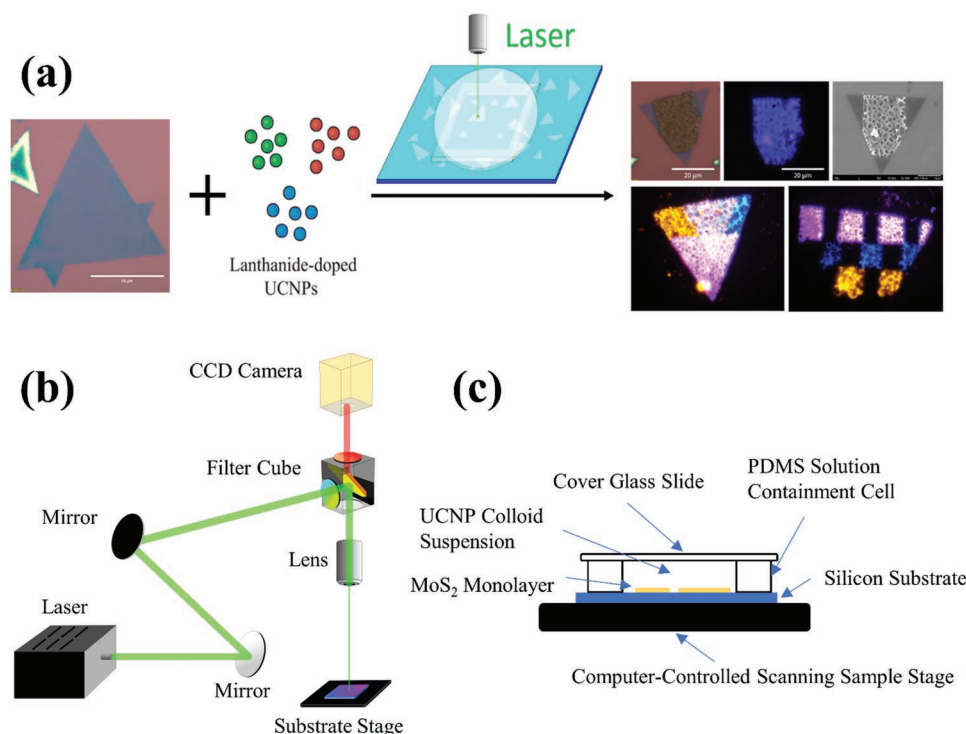
**ADVANCED
SCIENCE NEWS**
www.advancedsciencenews.com

**ADVANCED
MATERIALS
INTERFACES**
www.advmatinterfaces.de

Figure 1. Schematics for micropatterning experimental design and instrumental setup. a) UCNPs of variable emission colors and MoS$_2$ monolayers were produced and assembled into a solution cell device. Subsequent laser irradiation induces spatially selective aggregation of UCNPs on MoS$_2$ for micropatterning. b) Laser coupled microscope setup: laser beam directed and aligned through mirrors into filter cube. The beam was focused through an objective lens onto a solution cell and imaged via a CCD camera. c) Solution cell device: PDMS solution confinement cell emplaced atop as-grown MoS$_2$ monolayer on SiO$_2$/Si substrate. Cell topped with a transparent coverslip for laser penetration without severe solvent evaporation.

space group[44] of the hexagonal phase NaYF$_4$ and NaGdF$_4$ nanocrystals.

The MoS$_2$ monolayers utilized for this work were synthesized by two approaches: chemical vapor deposition (CVD) (Figure S2a, Supporting Information) growth assisted by a seed promoter—perylene tetracarboxylic acid tetrapotassium salt (PTAS)[45] or a melting point mediating precursor impurity—sodium chloride (NaCl).[46,47] The resultant monolayers with differential qualities were used to test the universality pertaining to the method. Both techniques produced quality MoS$_2$ monolayers with the regular triangular features defined by sharp edges and corners (Figure S2b,c, Supporting Information). Under fluorescence microscopy induced by yellow light (535–585 nm), the difference in quality was revealed. The PTAS grown MoS$_2$ triangles exhibit a bright red fluorescence that is uniform throughout the whole triangle. MoS$_2$ triangles grown in the presence of NaCl gave weaker fluorescence confined to the inner rim of its edges (Figure S2d,e, Supporting Information). Such differences in fluorescence intensity and distribution could be ascribed to heterogeneous distribution and disparate amounts of sulfur vacancies present in the monolayers.[48] Nonetheless, we expect both variants of MoS$_2$ monolayers to be still appropriate for UCNPs deposition and canvasing. Furthermore, the standard characterizations of Raman, photoluminescence, and atomic force microscope (AFM) mapping all assured the monolayer nature of the as-grown triangles. Since the wavenumber difference (Δk) between the A$_{1g}$ and E$_{2g}$ vibrational modes of MoS$_2$ was known to adjust

with the number of layers, the correlation of the measured difference at 19.2 cm^{-1} with the literature value[49] of 19.0 cm^{-1} was affirming of a monolayer feature (Figure S2f, Supporting Information). Moreover, with changes in band structure pertaining to the number of layers, the dominant photoluminescence (Figure S2g, Supporting Information) at 680.16 nm (1.8 eV) reiterates the monolayer nature of our grown triangles,[50] corroborated by the 0.7 nm sample thickness[51] in the AFM measurement (Figure S2h, Supporting Information) known to be characteristic of the height profile per monolayer MoS$_2$.

2.2. Production of UCNP/MoS$_2$ Hybrids: Laser-Assisted Microcanvas Formation

Upon irradiation of the scanning focused laser beam, localized UCNP aggregation and deposition was unexpectedly discovered to produce various microstructures on the MoS$_2$ monolayer surface. The presence of the laser beam amidst the liquid cell environment influenced the nanoparticle movement in solution, resulting in dynamic assembly and aggregation of UCNPs specifically at the laser–MoS$_2$ interface. As a result, UCNP clusters were controllably anchored on the MoS$_2$ surface, providing a microscale platform with high defined color resolution when driven by 980 nm excitation; analogous to a beautiful artform aptly described as a microcanvas.

In a stationary single spot exposure (**Figure 2**a–e), a ring microstructure was produced, comprising of high UCNP

**ADVANCED
SCIENCE NEWS**

www.advancedsciencenews.com

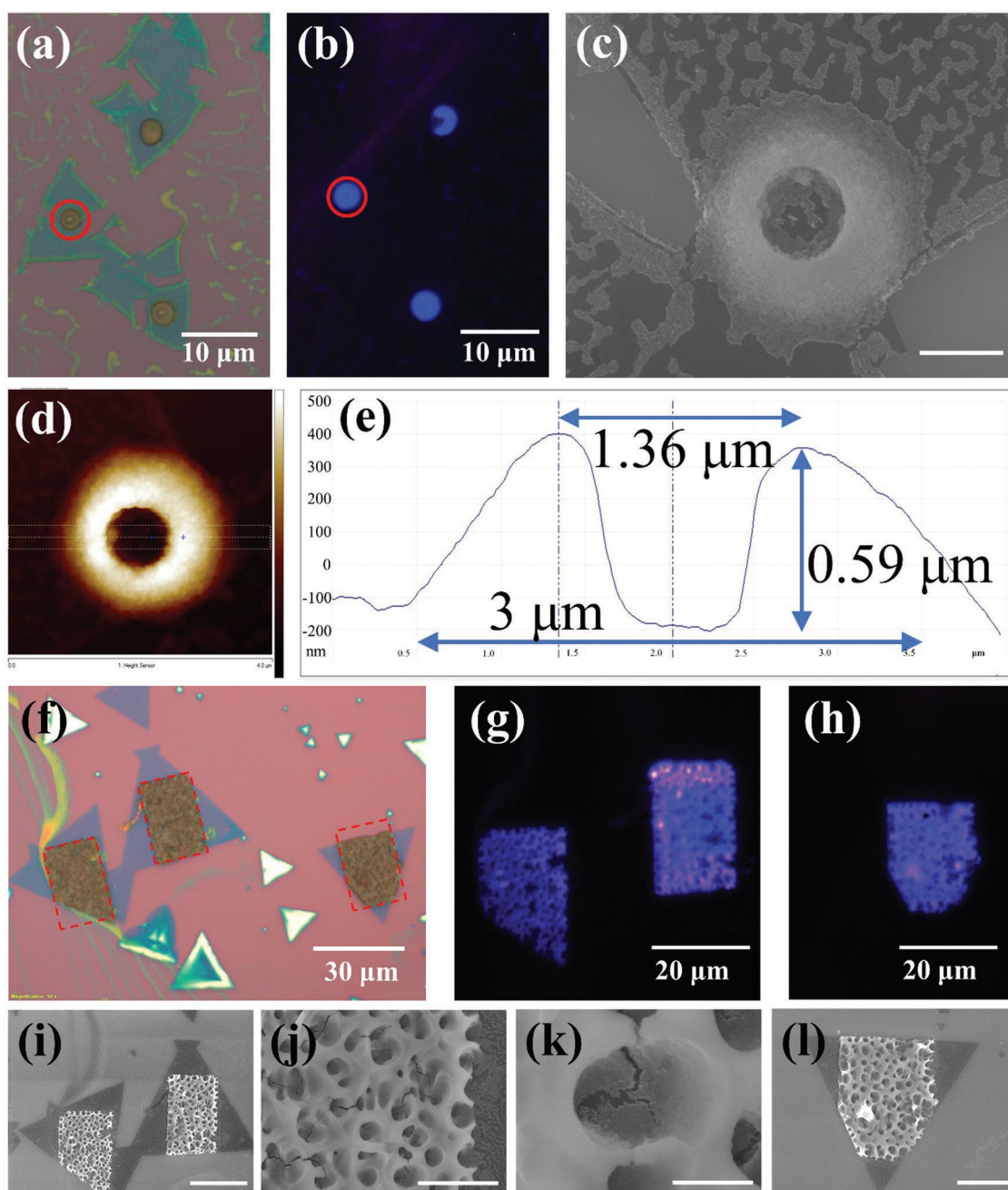**ADVANCED
MATERIALS
INTERFACES**

www.advmatinterfaces.de

Figure 2. Microstructures formed by laser-assisted UCNP deposition. a) Optical image of microrings produced from single spot laser exposure. b) Corresponding upconversion emission under 980 nm excitation. c) SEM image of microring site marked out by red circle in (a) and (b). Scale bar: 1 μm. d,e) AFM profiling of the same microring site with dimensions marked out in the cross-section profile. f) Optical image of sponge-like structures from raster scan laser exposure. Dashed red rectangles marked the regions of the laser raster scans. g,h) Corresponding upconversion emission under 980 nm excitation. i–l) SEM images of the sponge-like microstructures formed. Scale bar in images (i) 20 μm, (j) 5 μm, (k) 1 μm, and (l) 10 μm.

density stacked along the periphery with a cavity in the central region, as evident by SEM analysis. The central cavity comprised of a thin layer of UCNP deposit, surrounded by highly symmetrical circular wall stacks. Under subsequent AFM analysis, the dimensions of the microstructure were defined, reporting an overall 3 μm diameter coverage of the overall structure encompassing a 590 nm tall cavity with a peak to peak lateral distance of 1.36 μm. Upon irradiation with the

980 nm NIR laser, the ring structure revealed a purplish-blue hue (Figure 2b) characteristic of Eu^{3+}/Tm^{3+} ion emission from the variant of $NaGdF_4:Yb^{3+}/Tm^{3+}@NaGdF_4:Eu^{3+}$ nanoparticles deposited. This observation not only provides an insight into the microdisplay potential of the technique but also serves to validate the composition of the microstructure formed. When the laser was scanned by moving the sample in a raster fashion mechanically controlled by a micropositioner, the resultant
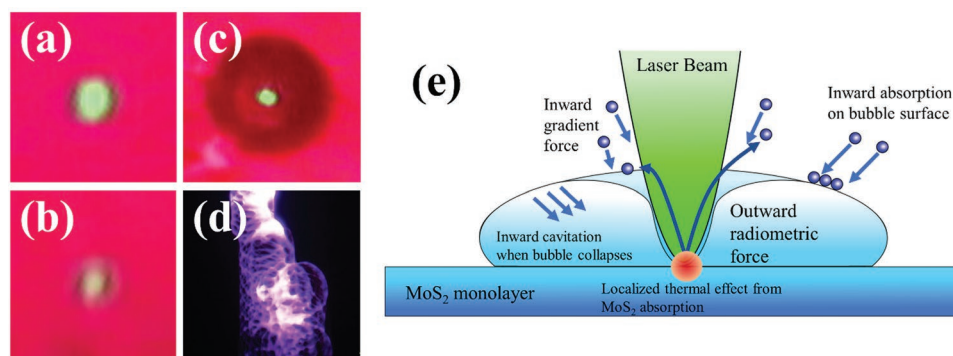
**ADVANCED
SCIENCE NEWS**

www.advancedsciencenews.com

**ADVANCED
MATERIALS
INTERFACES**

www.advmatinterfaces.de

Figure 3. Proposed mechanism for laser-guided UCNP deposition. a) Laser beam spot on a SiO$_2$ substrate. b) Laser beam spot on MoS$_2$ monolayer. The diffused concentric ring is observed around the main spot. c) Optical image of a huge bubble formation on slow and intense laser beam scan. d) Resultant UCNP feature from multiple large bubble formation—overlapping larger ring deposits formed. e) Schematics of laser-induced bubble formation and various forces at play contributing to the UCNP deposition process.

microstructure took the form of a sponge-like structure, characterized by clean cut, well-defined rectangular corners and edges (Figure 2f–l). This demonstrates the capability of the technique to produce defined patterns with resolution down to the micrometer range. SEM imaging of the rectangular block revealed multiple pores or potholes derived from the merger of many individual ring structures. Similarly, the upconversion emission (Figure 2g,h) from the microstructure was outstanding relative to the background, giving the clear distinction of the structure contours and outlines. Remarkably, as the laser rasters across a rectangular region (Figure 2f; red dashed rectangle boundaries) spanning beyond the triangular boundary of the MoS$_2$ monolayer, a clear distinction in the substrate selectivity was observed; the aggregation was dominant on MoS$_2$ surface, with close to none on the surrounding SiO$_2$ substrate despite having the laser scanned through as well. Consequentially, there exists very low background upconverted emission, coherent with the apparent contrast observed during upconversion imaging. Such substrate selectivity not only provided the basis for spatial control in the micropatterning, but also hinted toward the deposition mechanism at play. It is expected that differential interaction between the laser beam and the respective substrates (MoS$_2$ and SiO$_2$) influenced the dynamics of UCNP aggregation at these various sites.

2.3. Laser-Assisted Deposition: Mechanism

Previously, microring structures were successfully formed from experiments involving laser-induced aggregation of gold nanoclusters[52] or polystyrene particles[53] of rather substantial sizes. We expect that the physical mechanism contributed by the laser beam on the aggregation process to effectively be translatable to the system in this study. Serendipitously discovered in an earlier study on optical tweezing,[54] the phenomenon was accounted by a combination of inward radiation force at the laser beam waist with outward radiometric force at the beam center.[52] With the optical-based consolidation of particles at the periphery and the thermal induced dissipation at the core, the resultant ring structure was instantaneously produced. Furthermore, the thermal effect driven by the beam center could

essentially result in local heating up to a few hundred—degree Celsius, promoting convection or hydrodynamic drag[55] due to solvent heating or evaporation around the thermal hotspot, which would transport UCNPs away from the beam center and toward the beam circumference for deposition.

A simple comparison of the laser beam profile on SiO$_2$ (**Figure 3**a) against that on MoS$_2$ (Figure 3b) reveals a slightly more diffused beam profile when scanning on the surface of the MoS$_2$ monolayer; the defocusing of the laser beam distinctly presents a beam profile with a seemingly airy ring around the main beam center (Figure 3a,b; Movie S1, Supporting Information). When the laser was operated at higher powers and scanned at slower speeds, the beam profile became even more widespread, along with the formation of a bubble that continued to grow with extended laser exposure. Once subsided, the bubble leaves behind a thinner ring of UCNPs at a much larger radius, in comparison to that formed under optimal raster conditions (Figure 3c,d). Drawing relation between the two observations, we were inclined to believe that microbubbles were formed at the interface between the laser beam and MoS$_2$ surface, promoting the ring-shaped deposition of nanoparticles due to adhesion at the bubble surface. When the laser beam was incident on the sample, the light absorption by the MoS$_2$ monolayer resulted in a heated spot that rapidly vaporized the surrounding ethanol solvent to produce the bubble. The gas–liquid interface at the surface of the bubble provided sites for UCNP assembly whereas the local high-temperature hotspot promotes aggregation of the UCNPs, forming the microfeatures. Comparatively, bare SiO$_2$ is reflective of the incident laser beam and does not produce such a similar pronounced effect, resulting in the selective deposition only on the MoS$_2$ regions and not on the bare SiO$_2$ substrate areas. Bringing together all the mechanistic contributions discussed above, the overall schematic of the formation of the unit ring microstructure is as presented under Figure 3e.

Since the UCNPs utilized in this project are mainly hydrophilic, ligand-free variants, the influence of van der Waals (vdW) interactions at play should not be discounted. After the withdrawal of the laser source, the agglomerations formed were not only highly stable but were also found to accord impressive adhesion to the monolayer surface. The hybrid microstructures

ADVANCED
SCIENCE NEWS
www.advancedsciencenews.com

ADVANCED
MATERIALS
INTERFACES
www.advmatinterfaces.de

were resistant to multiple intensive washes in acetone and isopropanol. It is hence expected that both the laser beam and microbubble surface catalyzed the process of interparticle aggregation by greatly reducing the interparticle distances, producing microstructures strongly held by interparticle vdW forces. Afterward, a precise mechanical disruption using a fine tip 7 μm tungsten needle controlled by a micropositioning holder was accorded, eventually crumbling the UCNP assembly and revealing a relatively undisturbed MoS_2 monolayer beneath (Figure S3, Supporting Information). Fluorescence imaging of the recovered MoS_2 surface (Figure S3f, Supporting Information) displayed an intensity comparable to the initial state (Figure S3b, Supporting Information) before the deposition process. Since the optical activities of MoS_2 monolayers are known to be intimately dependent on its elemental stoichiometric ratio,[48] the result is a marked display of minimal influence on the chemistry of the monolayer. The adhesion was thus predominantly driven by physical adsorption, hinting a possibility of strong MoS_2–UCNP vdW attraction. Furthermore, the exposure of positively charged lanthanide ions on the surface of the ligand-free UCNP[56] complements the slightly n-doped nature of CVD grown MoS_2 monolayers, accounting the certain extent of electrostatic attractions to the secured adhesion. Together, these forces at play promote the nondestructive nature of the process with the implication of an entirely physical process in place, reinforcing the mechanism as discussed above.

Similar retention in optical properties of the MoS_2 monolayer was discovered in a reference experiment involving laser raster of the sample in pure ethanol (Figure S4, Supporting Information). Despite the absence of UCNPs in the solvent, the same microbubble and laser defocusing phenomenon was achieved (Movie S2, Supporting Information), indicating that the mechanism is independent of the solutes. The unchanged fluorescence of the monolayer proved unaltered surface chemistry and absence of laser-induced volatilization of the top sulfur layer; a piece of indirect evidence that the microbubbles do not comprise any sulfur content (sulfur vapor or oxidized SO_2) and therefore should consist of ethanol vapors only.

More than that, the microcanvasing technique was found to be universal across a wide range of parameters. Similar hybrid structures were found to be reproducible using either a 405 nm blue laser (Figure S5, Supporting Information) or other polar solvents (methanol (MeOH) (Figure S6, Supporting Information) and dimethylformamide (DMF) (Figure S7, Supporting Information)) instead. Under blue laser influence, the microstructures showed minimal morphological differences to that achieved under the green laser, proving the indifference in the microstructural construct of the hybrid formed under variable laser wavelengths. With variable solvent influence, it was notable that deposition conducted in DMF solvent was found to be less vigorous than that in MeOH and EtOH, producing a thinner, uniform layer of UCNPs in place of the usual porous 3D agglomeration (Figure S7, Supporting Information). The claim was supported by both AFM and SEM analyses describing a denser, coherent coating of UCNPs at lasered regions of the monolayer, with a vertical profile of 11.1 nm (Figure S7i, Supporting Information) in distinct contrast to that of 590 nm in microstructures produced in alcohol solvents. Due to the higher boiling point of DMF (153 °C) in comparison

to that of MeOH (64 °C) and EtOH (78 °C), it would be rational to expect that the decreased tendency for volatilization and violent bubble formation correlates with the gentler aggregation extent under DMF conditions. This reiterates the possibility of a bubble incited aggregation process influenced by the intensity and rate of bubble formation.

Under the influence of variable laser power, the microstructure topology was found to commensurate with the parameter changes. Under AFM evaluation, the density of UCNP deposition and hybrid surface roughness was found to be proportional to the laser power (Figure S8, Supporting Information). Such correlation demonstrated the importance of the laser intensity on the canvasing site. With a higher laser energy flux incident on the sample, the propensity for quicker and larger microbubble formation promoted a greater extent of UCNP deposition but at a more haphazard fashion; the resultant microstructure aggregations were more pronounced with taller height profile and greater surface roughness. The interconnection between laser operation parameters and the trend in microstructure features provided yet another supporting evidence of the microbubble induced mechanism at play.

2.4. UCNP/MoS₂ Hybrid Application: Micropattern Display

To evaluate the capability of the laser-induced deposition technique to produce micropatterned displays of high resolution and color capability, we subject the MoS_2 monolayer to multiple runs of deposition using UCNPs of different variants. As shown in **Figure** 4a–f, the extensive spatial control of the laser-induced patterning technique allows for the creation of array patterns comprising of various shapes formed using a variety of UCNPs. The resultant structures display similar features (sponge and ring like), proving the same mechanism at work that is invariant to the type of UCNPs utilized. Through repeated deposition runs on the same sample, it is possible to congregate different UCNPs onto a single monolayer for multicolor patterning. Herein, we produce an array of laser deposited squares capable of tricolor emission (Figure 4g), along with samples having an overlapping region of triangular deposits (Figure 4h–i). With the deposition area of each layer scan demarcated by the drawn triangle boundaries, we identified seven separate regions of contrasting upconversion emissions, four of which relates to overlapping regions of the triangular deposits (regions 2, 4, 6, 7 of Figure S9, Supporting Information). Through a spectroscopic study, individual regions were assessed to be spectroscopically different, with the four overlapping regions comprising emission peaks characteristic of the contributing UCNP colors. This provides an additional layer of patterning involving composite colors arising from a physical mix of UCNP types within the overlapping laser scan regions. Furthermore, with the flexible fine-tuning of UCNP emission profile by nanoparticle design and dopant variation, the potential for multicolor display involving colors spanning the whole color gamut would be well within reach.

Under the scrutiny of the SEM-EDX characterization, the surface topology of the multicolor UCNP deposited hybrid
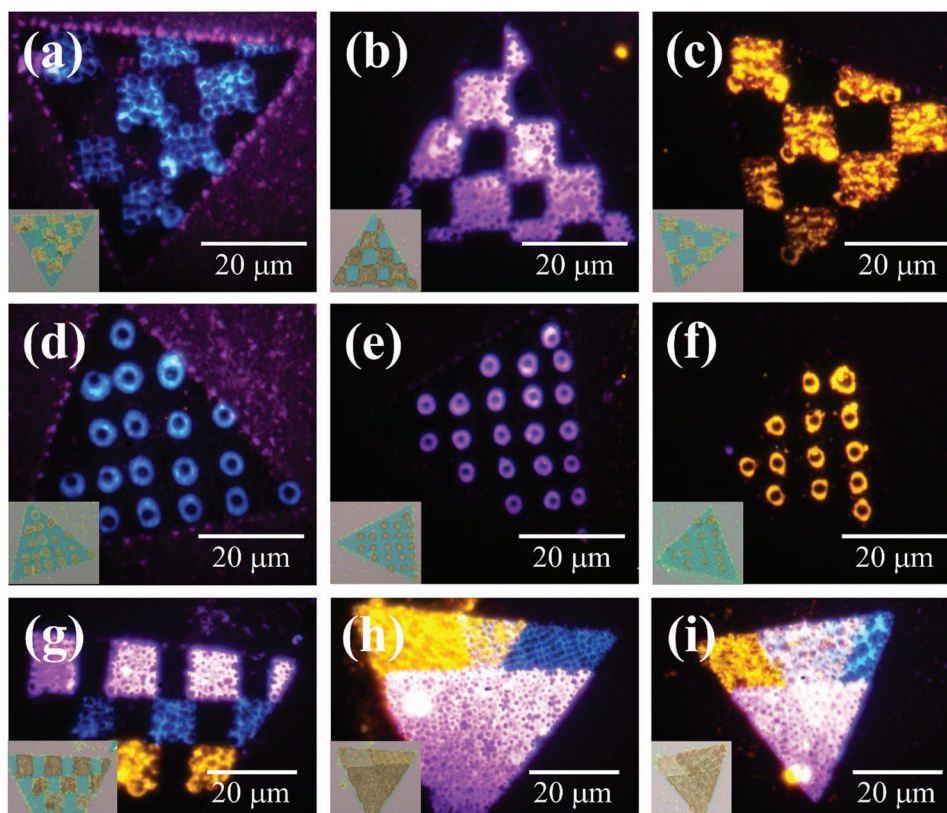
**ADVANCED
SCIENCE NEWS**
www.advancedsciencenews.com

**ADVANCED
MATERIALS
INTERFACES**
www.advmatinterfaces.de

Figure 4. UCNP/MoS$_2$ micropattern display. a–c) Upconversion imaging (λ_{ex} = 980 nm) of square arrays of various UCNP types patterned via raster laser scan atop of the MoS$_2$ monolayer: a) NaGdF$_4$:Yb^{3+}/Tm^{3+}@NaGdF$_4$:Tb^{3+} UCNPs. b) NaGdF$_4$:Yb^{3+}/Tm^{3+}@NaGdF$_4$:Eu^{3+} UCNPs. c) NaYF$_4$:Yb^{3+}/Er^{3+}@NaYF$_4$ UCNPs. d–f) Upconversion imaging of single spot ring arrays using the same variant of UCNPs as (a)–(c). g–i) Upconversion tricolor patterns from multiple step deposition onto single MoS$_2$ monolayer entities: (g) raster scan square arrays. (h,i) Overlapping large area triangular raster scan depositions for multicolor displays. Insets: optical images of the respective UCNP patterned samples.

was revealed to still retain a highly porous morphology (Figure S10a–d, Supporting Information). Relative to a singly rastered structure, the hybrid formed after multiple canvasing runs was found to display an increase in UCNP density and correspondingly reduced porosity. Since the former deposition run was expected to have UCNPs cover up most of the MoS$_2$ monolayer surface, it is reasonable that subsequent deposition atop the first UCNP layer is driven by laser-induced UCNP aggregation instead of a bubble-assisted mechanism. The results of EDX analysis (Figure S10e–j, Supporting Information) depicted distinct regions of high elemental concentrations that corroborated with specific compositions in the various UCNP variants, further reiterating the identities of the deposited microstructures and the highly defined boundaries pertaining to the precise technique.

3. Conclusion

In conclusion, we have demonstrated the ability of a laser directed microcanvasing system to anchor UCNPs at specific regions of a MoS$_2$ monolayer surface. Under a single spot laser exposure or raster laser scanning, various ring- and sponge-like microstructures were formed respectively. The laser induced

microbubble formation was predicted to facilitate nanoparticle aggregation, leading to the formation of colored arrays and multicolor structures. The technique was found versatile across a range of laser wavelengths and solvent medium. This marks the onset of a highly flexible method to interface various preassembled nanostructures, leading to a conceivable large pool of new functional hybrids.

Supporting Information

Supporting Information is available from the Wiley Online Library or from the author.

Conflict of Interest

The authors declare no conflict of interest.

Keywords

[1] D. Zhang, B. Gökce, S. Barcikowski, *Chem. Rev.* **2017**, *117*, 3990.
[2] H. Huang, J. Lai, *Proc. SPIE* **2018**, *10813*, 46.
[3] J. K. Hohmann, M. Renner, E. H. Waller, G. von Freymann, *Adv. Opt. Mater.* **2015**, *3*, 1488.
[4] J. Fischer, M. Wegener, *Laser Photonics Rev.* **2013**, *7*, 22.
[5] G. Yang, Y. Shen, *Proc. SPIE* **1998**, *3550*, 409.
[6] Z. Sekkat, S. Kawata, *Laser Photonics Rev.* **2014**, *8*, 1.
[7] K. Y. Lim, C. H. Sow, J. Lin, F. C. Cheong, Z. X. Shen, J. T. L. Thong, K. C. Chin, A. T. S. W. Wee, *Adv. Mater.* **2003**, *15*, 300.
[8] X. Lim, Y. Zhu, F. C. Cheong, N. M. Hanafiah, S. Valiyaveettil, C. H. Sow, *ACS Nano* **2008**, *2*, 1389.
[9] F. C. Cheong, B. Varghese, S. Sindhu, C. M. Liu, S. Valiyaveettil, A. A. Bettiol, J. A. Van Kan, F. Watt, W. S. Chin, C. T. Lim, C. H. Sow, *Appl. Phys. A* **2007**, *87*, 71.
[10] J. Gupta, X. Lim, C.-H. Sow, C. Vijayan, *J. Nanosci. Nanotechnol.* **2011**, *11*, 4029.
[11] B. Mukherjee, G. Murali, S. X. Lim, M. Zheng, E. S. Tok, C. H. Sow, *RSC Adv.* **2014**, *4*, 10013.
[12] Y. R. Choi, M. Zheng, F. Bai, J. Liu, E. S. Tok, Z. Huang, C. H. Sow, *Sci. Rep.* **2015**, *4*, 4940.
[13] J. Lu, X. Lim, M. Zheng, S. G. Mhaisalkar, C. H. Sow, *ACS Nano* **2012**, *6*, 8298.
[14] J. Lu, J. Wu, A. Carvalho, A. Ziletti, H. Liu, J. Tan, Y. Chen, A. H. Castro Neto, B. Özyilmaz, C. H. Sow, *ACS Nano* **2015**, *9*, 10411.
[15] J. Lu, J. Yang, A. Carvalho, H. Liu, Y. Lu, C. H. Sow, *Acc. Chem. Res.* **2016**, *49*, 1806.
[16] A. Venkatakrishnan, H. Chua, P. Tan, Z. Hu, H. Liu, Y. Liu, A. Carvalho, J. Lu, C. H. Sow, *ACS Nano* **2017**, *11*, 713.
[17] Y. C. Wan, H. F. Teoh, E. S. Tok, C. H. Sow, *J. Appl. Phys.* **2015**, *117*, 054304.
[18] J. Lu, J. H. Lu, H. Liu, B. Liu, L. Gong, E. S. Tok, K. P. Loh, C. H. Sow, *Small* **2015**, *11*, 1792.
[19] L. Gong, Q. Zhang, L. Wang, J. Wu, C. Han, B. Lei, W. Chen, G. Eda, K. E. J. Goh, C. H. Sow, *Nano Res.* **2018**, *11*, 4574.
[20] H. F. Teoh, P. Dzung, W. Q. Lim, J. H. Chua, K. K. Lee, Z. Hu, H. Tan, E. S. Tok, C. H. Sow, *Nanoscale* **2014**, *6*, 3143.
[21] S. X. Lim, G. K. W. Koon, Z. Zhang, A. H. Castro Neto, E. S. Tok, C. H. Sow, *Nanoscale* **2018**, *10*, 18145.
[22] S. X. Lim, Y. Z. Lee, N. Gao, J. Lu, Q. Xu, E. S. Tok, C. H. Sow, *J. Mater. Chem. C* **2018**, *6*, 4641.
[23] M. H. R. Seah, S. X. Lim, E. S. Tok, C. H. Sow, *J. Lumin.* **2019**, *205*, 357.
[24] A. V. Povolotskaya, M. A. Lesik, A. V. Povolotskiy, A. A. Manshina, *IEEE* **2009**, *163*, 1.
[25] L. Nanai, A. M. Balint, *AIP Conf. Proc.* **2012**, *1472*, 148.
[26] P. Alonso-Cristobal, P. Vilela, A. El-Sagheer, E. Lopez-Cabarcos, T. Brown, O. L. Muskens, J. Rubio-Retama, A. G. Kanaras, *ACS Appl. Mater. Interfaces* **2015**, *7*, 12422.
[27] J. Lv, S. Zhao, S. Wu, Z. Wang, *Biosens. Bioelectron.* **2017**, *90*, 203.
[28] N. Zhou, B. Xu, L. Gan, J. Zhang, J. Han, T. Zhai, *J. Mater. Chem. C* **2017**, *5*, 1591.
[29] W. Niu, H. Chen, R. Chen, J. Huang, H. Sun, A. I. Y. Tok, *Chem. Commun.* **2015**, *51*, 9030.
[30] Y. Zhang, J. Wang, B. Wang, J. Shao, J. Deng, C. Cong, L. Hu, P. Tian, R. Liu, S. L. Zhang, Z. J. Qiu, *Adv. Opt. Mater.* **2018**, *6*, 1800660.
[31] M. Chatti, V. N. K. B. Adusumalli, S. Ganguli, V. Mahalingam, *Dalton Trans.* **2016**, *45*, 12384.
[32] Y. Zhai, X. Yang, F. Wang, Z. Li, G. Ding, Z. Qiu, Y. Wang, Y. Zhou, S. T. Han, *Adv. Mater.* **2018**, *30*, 1803563.
[33] W. J. Kim, M. Nyk, P. N. Prasad, *Nanotechnology* **2009**, *20*, 185301.
[34] T. Blumenthal, J. Meruga, P. Stanley May, J. Kellar, W. Cross, K. Ankireddy, S. Vunnam, Q. N. Luu, *Nanotechnology* **2012**, *23*, 185305.
[35] J. M. Meruga, W. M. Cross, P. Stanley May, Q. Luu, G. A. Crawford, J. J. Kellar, *Nanotechnology* **2012**, *23*, 395201.
[36] J. M. Meruga, A. Baride, W. Cross, J. J. Kellar, P. S. May, *J. Mater. Chem. C* **2014**, *2*, 2221.
[37] M. You, J. Zhong, Y. Hong, Z. Duan, M. Lin, F. Xu, *Nanoscale* **2015**, *7*, 4423.
[38] F. Wang, R. Deng, X. Liu, *Nat. Protoc.* **2014**, *9*, 1634.
[39] D. Li, Q. Shao, Y. Dong, J. Jiang, *J. Rare Earths* **2014**, *32*, 1032.
[40] J. F. Suyver, A. Aebischer, D. Biner, P. Gerner, J. Grimm, S. Heer, K. W. Krämer, C. Reinhard, H. U. Güdel, *Opt. Mater.* **2005**, *27*, 1111.
[41] F. Wang, X. Liu, *Chem. Soc. Rev.* **2009**, *38*, 976.
[42] F. Wang, R. Deng, J. Wang, Q. Wang, Y. Han, H. Zhu, X. Chen, X. Liu, *Nat. Mater.* **2011**, *10*, 968.
[43] J. Zhou, Q. Liu, W. Feng, Y. Sun, F. Li, *Chem. Rev.* **2015**, *115*, 395.
[44] F. Wang, Y. Han, C. S. Lim, Y. Lu, J. Wang, J. Xu, H. Chen, C. Zhang, M. Hong, X. Liu, *Nature* **2010**, *463*, 1061.
[45] X. Ling, Y. H. Lee, Y. Lin, W. Fang, L. Yu, M. S. Dresselhaus, J. Kong, *Nano Lett.* **2014**, *14*, 464.
[46] S. Li, S. Wang, D. M. Tang, W. Zhao, H. Xu, L. Chu, Y. Bando, D. Golberg, G. Eda, *Appl. Mater. Today* **2015**, *1*, 60.
[47] Z. Jiadong, L. Junhao, H. Xiangwei, Z. Yao, C. Yu, X. Juan, W. Hong, X. Yu, Y. Huimei, L. Jincheng, W. Di, L. Fucai, F. Qundong, Z. Qingsheng, H. Chuang-Han, Y. Changli, L. Li, Y. Ting, S. Zexiang, L. Hsin, Y. Boris I., L. Qian, S. Kazu, L. Guangtong, Z. Liu, *Nature* **2018**, *556*, 355.
[48] H. Liu, J. Lu, K. Ho, Z. Hu, Z. Dang, A. Carvalho, H. R. Tan, E. S. Tok, C. H. Sow, *Nano Lett.* **2016**, *16*, 5559.
[49] H. Li, Q. Zhang, C. C. R. Yap, B. K. Tay, T. H. T. Edwin, A. Olivier, D. Baillargeat, *Adv. Funct. Mater.* **2012**, *22*, 1385.
[50] A. Zafar, H. Nan, Z. Zafar, Z. Wu, J. Jiang, Y. You, Z. Ni, *Nano Res.* **2017**, *10*, 1608.
[51] J. Qi, Y. W. Lan, A. Z. Stieg, J. H. Chen, Y. L. Zhong, L. J. Li, C. D. Chen, Y. Zhang, K. L. Wang, *Nat. Commun.* **2015**, *6*, 7430.
[52] Y. Zhang, C. Gu, A. M. Schwartzberg, S. Chen, J. Z. Zhang, *Phys. Rev. B* **2006**, *73*, 165405.
[53] A. Haldar, S. B. Pal, B. Roy, S. D. Gupta, A. Banerjee, *Phys. Rev. A* **2012**, *85*, 033832.
[54] S. Sato, Y. Harada, Y. Waseda, *Opt. Lett.* **1994**, *19*, 1807.
[55] C. Shi, C. Zhang, C. Gu, L. Seballos, J. Z. Zhang, *Nanotechnology* **2008**, *19*, 215304.
[56] B. Nicoleta, V. Fiorenzo, G. A. Ozin, J. A. Capobianco, *Nano Lett.* **2011**, *1*, 835.